Global Navigational Satellite System Seismic Monitoring

Timothy I. Melbourne*[1], Walter M. Szeliga[1], Victor Marcelo Santillan[1], and Craig W. Scrivner[1]

ABSTRACT

We have developed a global earthquake deformation monitoring system based on subsecond-latency measurements from ~2000 existing Global Navigational Satellite System (GNSS) receivers to rapidly characterize large earthquakes and tsunami. The first of its kind, this system complements traditional seismic monitoring by enabling earthquake moment release and, where station density permits, fault-slip distribution, including tsunamigenic slow slip, to be quantified as rupture evolves. Precise point position time series from globally distributed GNSS stations are continuously estimated within an Earth center of mass-fixed reference frame and streamed as local north, east, and vertical coordinates with 1 s updates and global subsecond receiver-to-positions latency. Continuous waveforms are made available via messaging exchanges to third-party users (U.S. Geological Survey, National Oceanic and Atmospheric Administration, network operators, etc.) and internally filtered to trigger coseismic offset estimation that drive downstream point-source and finite-fault magnitude and slip characterization algorithms. We have implemented a corresponding analytics system to capture ~100 million positions generated per day per thousand global stations positioned. Assessed over one typical week using 1270 globally distributed stations, the latency of position generation at a central analysis center from time of data acquisition in the field averages 0.52 s and is largely independent of station distance. Position variances from nominal in north, east, and vertical average 8, 9, and 12 cm, respectively, predominantly caused by random-walk noise peaking in a ~4–5 min spectral band introduced by global satellite clock corrections. Solutions completeness over the week within 0.5, 1, and 2 s latency is 55%, 90%, and 99%, respectively. This GNSS analysis platform is readily scalable, allowing the accelerating proliferation of low-cost phase-tracking GNSS receivers, including those increasingly embedded in consumer devices such as smartphones, to offer a new means of characterizing large earthquakes and tsunami far more quickly than existing systems allow.

KEY POINTS

- We present an operational global, Global Navigational Satellite System (GNSS)-based seismic monitoring system.
- Subsecond-latency positioning from global stations enables ultrafast earthquake and tsunami characterization.
- This scalable and rapidly growing system offers a new method for global monitoring of earthquakes and tsunami.

INTRODUCTION

As earthquake fault rupture exceeds tens of kilometers in spatial extent and several seconds in duration, the complexity of *P* and *S* waveforms recorded on local seismometers, coupled with their extended coda and amplitude saturation on inertial seismometers, makes accurate magnitude determination and rupture distribution difficult to constrain using only local seismic arrays. Point-source amplitude–magnitude relationships generally grow less reliable as rupture length increases, but even distributed slip-estimation strategies are challenged for complex ruptures in which slip either changes rake along the propagation path (e.g., 2002 M_w 7.9 Denali earthquake), jumps multiple faults (e.g., 2019 M_w 7.1 Ridgecrest and 2016 M_w 7.9 Kaikoura earthquakes), comprises dynamic triggering that blurs subevents within rapid-fire foreshock–mainshock–aftershock sequences (e.g., 1954 Fairview Peak–Dixie Valley sequence), or, for earthquakes with slow rupture that radiate less power in seismic frequencies typically used to gauge magnitude (Kanamori and Kikuchi, 1993; Satake, 1995; Caskey *et al.*, 1996; Aagaard *et al.*,

1. Pacific Northwest Geodetic Array, Department of Geological Sciences, Central Washington University, Ellensburg, Washington, U.S.A., https://orcid.org/0000-0003-1870-3962 (TIM); https://orcid.org/0000-0002-9991-1204 (WMS)

*Corresponding author: tim@geology.cwu.edu

Cite this article as Melbourne, T. I., W. M. Szeliga, V. Marcelo Santillan, and C. W. Scrivner (2021). Global Navigational Satellite System Seismic Monitoring, *Bull. Seismol. Soc. Am.* **111**, 1248–1262, doi: 10.1785/0120200356

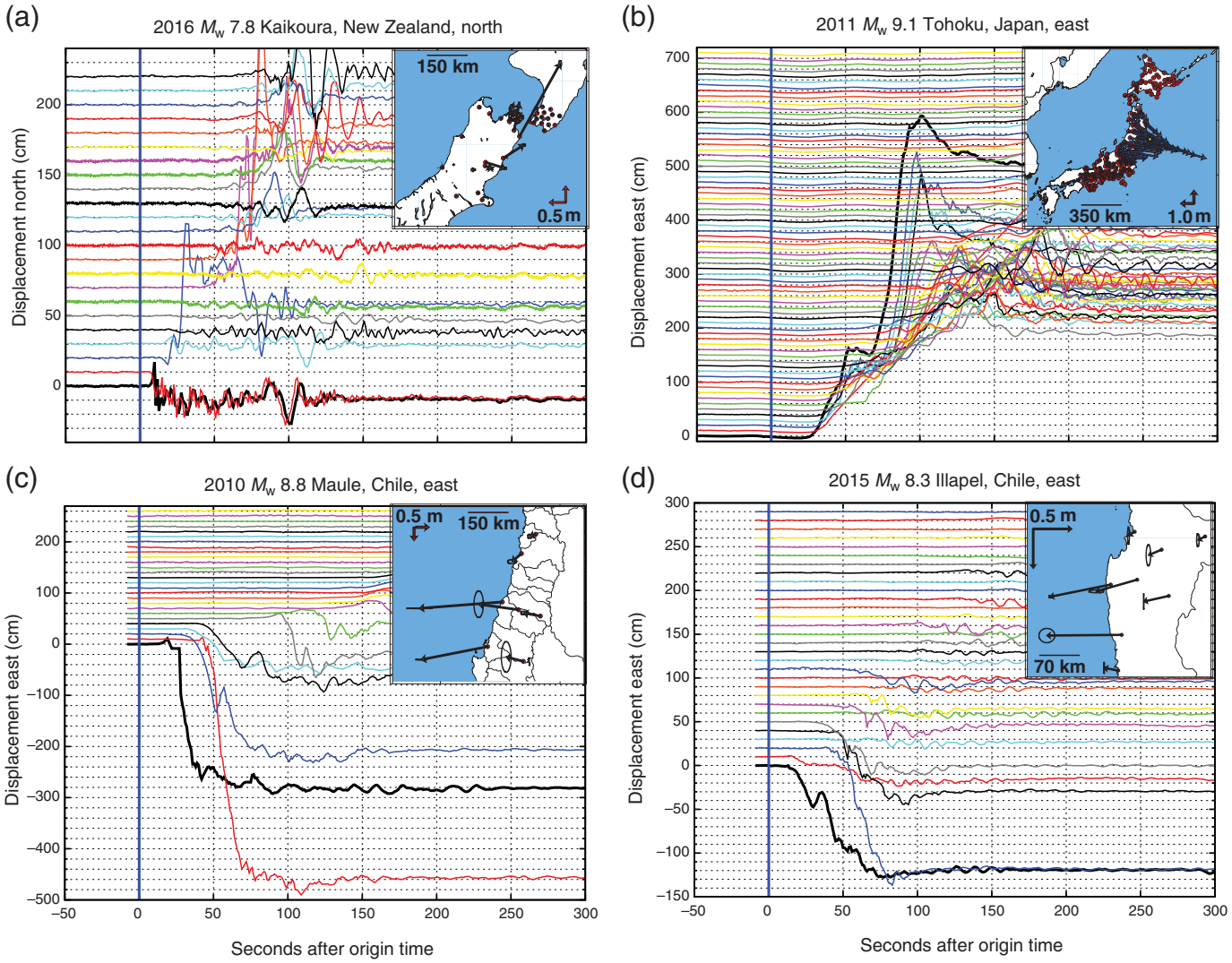

Figure 1. Global Navigational Satellite System (GNSS) position waveform time series and coseismic offsets (inset) for the (a) 2016 M_w 7.8 Kaikoura, New Zealand, (b) 2011 M_w 9.1 Tohoku, Japan, (c) 2010 M_w 8.8 Maule, and (d) 2015 M_w 8.3 Illapel, Chile, earthquakes. Traces that show the component of motion with the largest coseismic offset are sorted by increasing distance from epicenter and are offset vertically for clarity. Blue lines indicate even origin time; each receiver position trace is colored separately. Note differences in *y*-axis scales and component of motion shown. Tohoku point positions processed by Central Washington University, others from Ruhl *et al.* (2018).

2004; Barnhart *et al.*, 2019; Ross *et al.*, 2019). Strong ground motion early warning systems, such as SASMEX and ShakeAlert, also require accurate magnitude assessment within seconds to best determine where to, and not to, warn (Allen and Ziv, 2011) or to issue updated revisions for events for which rupture duration exceeds the window within which warnings must be issued to be of any use, typically just a few seconds (Espinosa-Aranda *et al.*, 2011; Given *et al.*, 2018; Hodgkinson *et al.*, 2020).

Real-time measurements from Global Navigational Satellite System (GNSS, of which the United States' Global Positioning System [GPS] was an early constellation) now offer a complementary solution to these deficiencies, for several reasons. First, near-field coseismic offsets grow linearly with respect to moment, rather than moment rate (which controls far-field waveforms), so saturation limits that hamper peak acceleration or velocity assessment of earthquake magnitude do not apply (Aki and Richards, 1980). In fact, modern GNSS receivers operating at high rate have been shown to not lose carrier phase or ranging lock until ground accelerations exceeded 4*g* at 5 Hz (Ebinuma and Kato, 2012; Berglund *et al.*, 2015). Assuming receiver power and telemetry can be kept on, which held true for the Japan GEONET array during the 2011 M_w 9 Tohoku event, despite widespread shaking intensity 6 and 7 reaching over 400 km along coastal Honshu (Hoshiba *et al.*, 2011), the signal-to-noise ratio of position resolution increases as motion amplitude increases toward arbitrarily large values. Second, near-field coseismic offsets start with the arrival of *P* wave, typically tens of seconds after origin time, depending on distance (Fig. 1). Dynamic displacements are initially superimposed on static

offsets, which delay accurately assessing them. In practice, magnitude can be accurately assessed nearly as moment is released, if there are near-field stations throughout the rupture. Moreover, dynamic displacements also carry valuable magnitude information that allows some algorithms to converge on a reasonably accurate magnitude, even before the rupture source time function is complete (Melgar and Hayes, 2019). Third, GNSS measures local long-period deformation without the intrinsic physical ambiguity between resolving tilt and acceleration that force-balance seismometers experience (Larson *et al.*, 2003). For all of these reasons, low-latency GNSS measurements can rapidly characterize large earthquakes that challenge traditional seismic analysis based on local seismometer networks. Figure 1 shows four large earthquakes well recorded with local GNSS measurements ranging in moment magnitude from M_w 7.8 to 9.1. For all of the events, even the 2011 M_w 9.1 Tohoku earthquake, coseismic offsets are nearly completely developed within 90 s of origin time, as has been previously noted, and far lower receiver density than is offered by Japan's GEONET array is needed to effectively constrain moment (Wright *et al.*, 2012). The basic requirements are that near-field GNSS stations exist, that their continuous data are available and shared in real time, that power and telemetry are uninterrupted in the presence of strong ground motion, and that positioning of raw satellite observables continues uninterrupted during and following the event. All of these requirements have proven to be true for over a dozen large events over the past decade (Ruhl *et al.*, 2018).

To date, however, integrating GNSS into seismic monitoring has proven tricky, for a host of reasons. First, GNSS receiver positions must be continuously inverted from the basic satellite observables of microwave carrier phase and range acquired at a receiver, which involves time-dependent observation and state evolution models. Unlike an inertial seismometer that outputs counts proportional to either an inductive voltage or a force-balance current linearly related to ground velocity, the north, east, and vertical components of a GNSS position are three of several parameters that must be continuously estimated, in a least-squares sense, from raw satellite observables, all of which trade-off with each other (Blewitt *et al.*, 1992). Each position estimate within a GNSS position time series is analogous to an earthquake hypocenter estimated from source-seismometer ranges defined by measured *S-P* travel times and a seismic velocity model. The need to coevaluate GNSS positions simultaneously with their covariances with other estimated parameters has proven to be a recurring source of difficulty in integrating GNSS into traditional seismic monitoring.

Nonetheless, GNSS monitoring has steadily been added in to traditional seismometer-based monitoring. One early application exploited relative positioning and the expected right-lateral rupture along the southern San Andreas fault to monitor baseline length changes (Hudnut *et al.*, 2002). Grapenthin *et al.* (2014a) developed an operational real-time system to also use real-time kinematic (RTK) positioning to supplement seismic monitoring for earthquake early warning applications in the Bay Area of California and with it captured the 2014 M_w 6.0 earthquake (Grapenthin *et al.*, 2014a,b). Kawamoto *et al.* (2016) obtained finite-fault estimations and a magnitude assessment of 6.8 within 1 min of origin time for the 2015 Kumamoto earthquake, which converged to its official M_J magnitude of 6.96 within 5 min. For ShakeAlert, the U.S. Geological Survey (USGS) ShakeAlert revised technical implementation plan calls for the integration of GNSS to guide subsequent alert updates for events for which rupture time persists longer than initial window within which initial alerts must be issued (Given *et al.*, 2018). For tsunami, 80% of which over the past century were caused by earthquakes, inundation can start within minutes, a far shorter interval than the propagation delay inherent to using teleseismic waveforms to constrain basic earthquake rupture, or waiting for Deep-ocean Assessment and Reporting of Tsunamis (DART) or tide gauges to detect the propagating wave itself (Kong *et al.*, 2015; Angove *et al.*, 2019). For this reason, the potential of global real-time GNSS to speed up local tsunami characterization has been repeatedly noted (Sobolev *et al.*, 2007; Song, 2007; Blewitt *et al.*, 2009; Melgar and Bock, 2013). In Japan, Ohta *et al.* (2012) have devised an operational near-field tsunami forecasting system for Japan, based on RTK GNSS positioning.

This article describes the analysis framework of a global, real-time, subsecond latency, GNSS crustal deformation monitoring system. It can ingest raw GNSS data acquired at any telemetered receiver on earth, position those data, and retransmit resulting positions to any Internet-connected device anywhere on earth, all with subsecond latency between the time of acquisition of raw satellite observations in the field and generation of a resulting position in Washington State. The emphasis on ultrafast protocols stems from the demands of earthquake early warning applications, in which every second matters, but it is equally useful as an ultrafast means of diagnosing tsunami excitation in coastal events. GNSS data and solutions are sufficiently different from existing digital seismometry that adapting them to seismic monitoring has required the development of entirely new positioning strategies and new streaming protocols needed to share both raw data and resultant position solutions worldwide with subsecond latency. This framework is mature and time tested, and has been running concurrently within the Pacific Northwest Geodetic Array at Central Washington University (CWU) since 2016. We discuss station distribution and access, telemetry, real-time point positioning, solutions retransmission, and coseismic offset detection. We also describe solution analytics designed to gauge accuracy, latency, and completeness for globally distributed GNSS station positions. We provide only an overview of the complexities of real-time GNSS point positioning, and we do not discuss the myriad downstream geophysical algorithms currently under development to invert

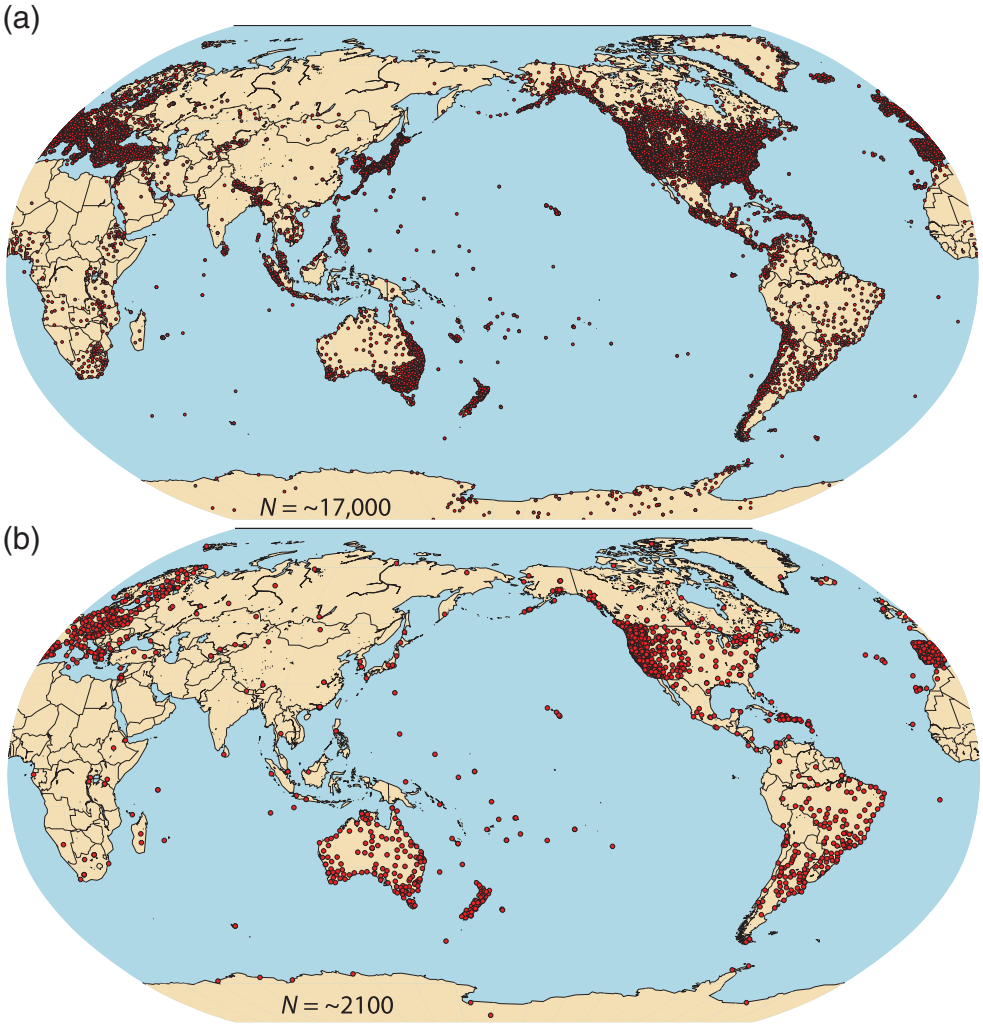

Figure 2. GNSS station maps. (a) Locations of all points on earth for which GNSS measurements have been acquired, as reflected by the processed positions repository at the University of Nevada, Reno, totaling over 18,000 monuments (Blewitt *et al.*, 2018). Only a small fraction of these are continuously monitored with low-latency telemetry and publicly available for hazards monitoring. (b) Continuously monitored and telemetered, publicly available receivers surveyed in 2020 yielded ~2100 available stations.

GNSS position waveforms and coseismic offsets for rupture parameters. These are well underway, and current approaches range from monitoring baselines across specific structures or active tectonic regions (Hudnut *et al.*, 2002; Grapenthin *et al.*, 2014b), empirical peak ground displacement (PGD)–distance magnitude relationships (Crowell *et al.*, 2013; Melgar *et al.*, 2015; Ruhl *et al.*, 2018), point-source and finite-fault continuous inversions (Crowell *et al.*, 2012), Bayesian distributed faulting (Minson *et al.*, 2014), and others. All of these algorithms rely on the generation of high-accuracy GNSS positions from around the globe and delivered with minimal latency.

GNSS COSEISMIC WAVEFORMS

Figure 1 shows GNSS position record sections from four large earthquakes—the 2010 M_w 8.8 Maule and 2015 Illapel, Chile, subduction events, the pathologically complex 2016 M_w 7.9 Kaikoura, New Zealand, earthquake, and the 2011 M_w 9.0 Tohoku, Japan, events (Ruhl *et al.*, 2018). Position time series for all events show clearly resolved coseismic deformation evolving quickly after nucleation, well prior to termination of their source time functions, as pointed out by Melgar and Hayes (2019). The magnitude high-8 and low-9 nature of these events is readily identified visually by meters of offset spanning hundreds of kilometers within 90 s, well in advance of availability of both the global *W*-phase moment estimate (Hayes *et al.*, 2011) as well as the time that most earthquake-induced local tsunami inundation began. Simple elastic half-space inversions or PGD-type algorithms easily capture the coarse magnitude within a few tens of seconds.

GLOBAL GNSS NETWORKS

Deployment of the majority of real-time networks worldwide today is driven by commercial land-surveying applications rather than basic science or hazards mitigation. However, because many surveying applications require real-time data to enable precise kinematic positioning, many of these stations can be adapted to seismic monitoring if data are shared for this purpose. Moreover, the rapid proliferation of GNSS networks over the past decade is likely to continue as networks in support of land surveying increase and also as consumer devices such as smartphones that are equipped with GNSS carrier-phase tracking capability proliferate (Minson *et al.*, 2015). Figure 2a shows stations post-processed for at least one day by the University of Nevada Reno Geodesy Laboratory archive, over 17,000 measurements in total (Blewitt *et al.*, 2018). These include any point measured with GNSS, which are far more abundant than continuously operating stations with real-time telemetry. Of these, the number of continuously operating GNSS stations worldwide is difficult to tally, because many networks operate on a

cost-recovery basis, which results in inconsistent public sharing of data. A 2019 scan of public-facing GNSS data casters with available stations yielded ~2200 stations that are publicly available in real-time feeds of high-rate (1 s) measurements (Fig. 2b). Along the US west coast within the ShakeAlert footprint, there are several operating networks, all of which data is publicly shared (Murray *et al.*, 2018). Globally, open-data access is more the exception than the rule at the present time, but international efforts are underway through the United Nations aiming for open GNSS data sharing for the purposes of hazards reduction (LaBrecque *et al.*, 2019).

PRECISE POINT POSITIONING (PPP) IN REAL TIME

GNSS positioning is a discipline unto itself, and detailed explorations of its many and varied facets can be found in Leick *et al.* (2015). For the purpose of understanding GNSS seismic monitoring, a receiver's position must be estimated at every epoch from the raw satellite observables acquired in the field, which typically comprise a minimum of two ranging and two phase observables per satellite in view, per epoch. The ranging measurement is obtained by cross correlating a message encoded on a carrier frequency transmitted by a satellite with that of a local copy generated at the receiver. The apparent range between the receiver and satellite is the time lag multiplied times the speed of light, but this measurement is biased by timing errors from the receiver and satellite clocks and by propagation delays through the earth's atmosphere, among other error sources, and is, therefore, called pseudorange. A second observable, the accrued phase of the carrier signal over an epoch, provides a more precise ranging measurement, if the initial carrier phase ambiguity can be resolved in a timely fashion (Blewitt *et al.*, 1992). Once receiver-satellite ranges are determined for a minimum number of satellites, the receiver's position is continuously inverted from these ranges, given knowledge of the satellite trajectories.

Both GNSS relative positioning (called RTK) and absolute, or PPP can be used for seismic monitoring. RTK was the predominant positioning approach for the first several decades for studying earthquakes with GNSS (Larson *et al.*, 2003; Larson, 2019). In this technique, one or more reference receivers are held fixed and nearby receiver positions are computed along baselines relative to the reference position. The advantages of relative positioning are that some positioning error sources cancel completely, including satellite orbit and onboard clock errors. Over short baselines (~50 km or less), other relative positioning error sources, such as tropospheric water and ionosphere electron content, cancel partially depending on their spatial gradient and the separation distance between target and reference receivers. Grapenthin *et al.* (2014b) describe the successful integration based on the TrackRT software (Herring, 2002) into the Berkeley Seismological Laboratory operations. For earthquake monitoring applications, however, relative positioning techniques will fail for large earthquakes, because the reference stations will move significantly before coseismic offsets are fully developed, depending on reference receiver location with respect to slip centroid. One solution is to invert for independent baselines (Grapenthin *et al.*, 2014a), but uncorrelated noise grows faster than coseismic deformation drops with distance, so, for large earthquakes, it is not possible to put reference stations far enough away to not be susceptible to aliasing of coseismic motion of the reference station. Another drawback is that the differencing operators inherent to relative positioning scale computationally as N^2, and so for very large or dense networks require division into and subsequent remerging of subnetworks.

The other approach, adopted here, is PPP, in which station position is estimated not relative to a nearby station but within a global reference frame defined by earth center of mass and the ephemerides of the satellites (Zumberge *et al.*, 1997). In this technique, satellite orbits, clocks, and earth orientation parameters are not solved for but are held fixed to values derived independently from global analyses and downloaded continuously as ancillary data products used in positioning. However, unlike in earthquake location (for which the seismic velocity structure is usually assumed to be unchanging), GNSS signal propagation delays through earth's ionosphere and troposphere change continuously and, therefore, must be also continuously accounted for. Signal propagation delay caused by the hydrostatic component of the troposphere, for instance, is generally equivalent to 2–3 m of apparent ground position at zenith and ~10 m at the horizon but varies only slightly with atmospheric pressure changes. Delay caused by tropospheric water, however, is only equivalent to a few tens of centimeters but varies strongly with the weather, as integrated water vapor content changes, and so must also be estimated alongside receiver position. Mismodeled tropospheric or ionospheric electron density variation will usually be absorbed by other variables in the estimation and so will manifest itself as apparent, but spurious, receiver position changes. Therefore, this must be discriminated for using solution covariances that are not readily incorporated into traditional seismic analysis systems.

The noise level for point positioning is higher than RTK over short baselines, but as ancillary data products and global atmospheric noise models improve, so too does the accuracy of absolute positioning (Geng *et al.*, 2019). For the largest earthquakes, PPP is preferable, because signal-to-noise resolution ramps up as deformation grows, while nearby reference stations cannot be assumed to be unmoving. PPP also has the advantage of being computationally efficient because CPU usage scales linearly with the number of stations by operating on only one receiver's data. PPP does not require the computation resources that the differencing of observables between receivers used in relative positioning requires and so is readily parallelized.

Figure 3 shows a flowchart of CWU's PPP framework. GNSS receivers in the field telemeter raw data to centralized

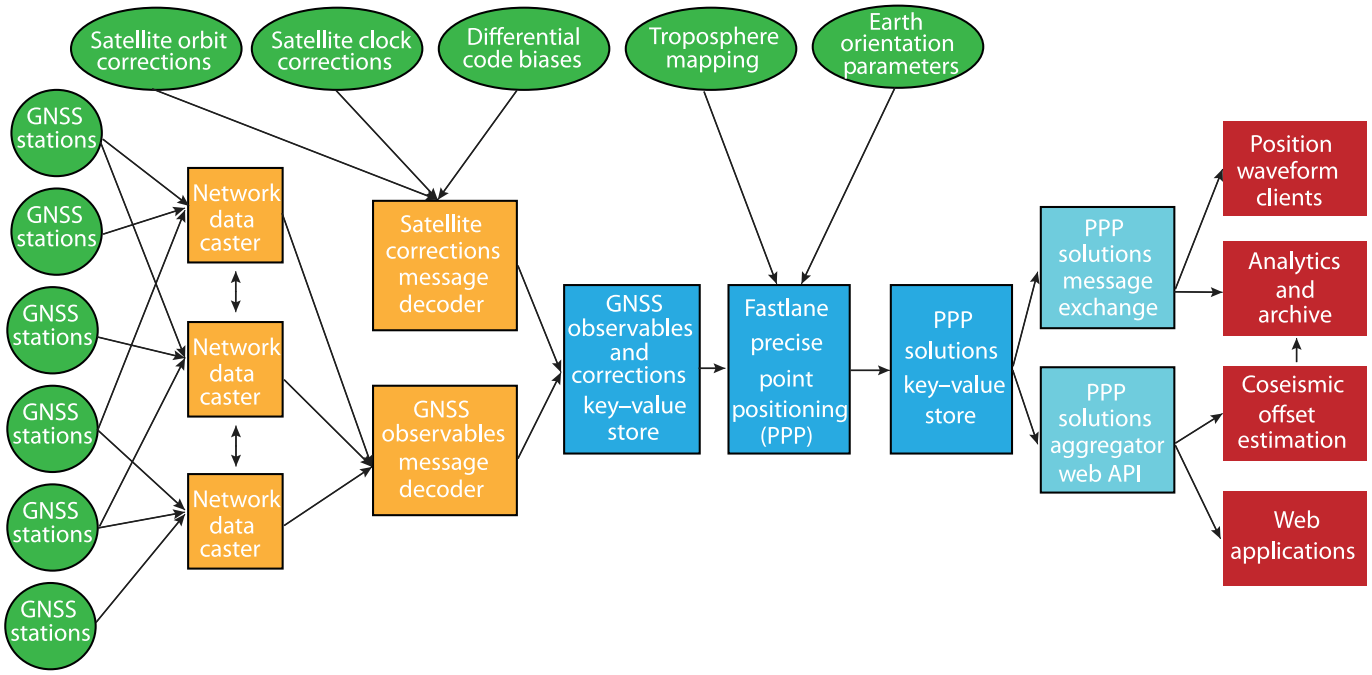

Figure 3. Flowchart of Central Washington University (CWU) GNSS positioning framework. Data from globally distributed GNSS networks are streamed from network casters into CWU, decoded, and stored in a high-speed key–value store. Satellite orbit and clock corrections, and differential code biases are streamed from the International GNSS Service (Dow *et al.*, 2009), decoded, and stored in a corrections key–value store. Fastlane positioning ingests observables and corrections, and streams precise point positioning (PPP) solutions to a downstream key–value store. Position waveforms are published through a messaging exchange to subscribed position waveform clients as well as for analytics and archive. Positions are also published through a second mechanism comprising a public-facing solutions aggregator. A separate Application Programmer Interface (API) is available to construct downstream web applications such as the GPSCockpit (Fig. 5) that connect to the aggregator to stream in waveforms, positions, and other derived products.

network casters that then rebroadcast the data to subscribed third parties. Dedicated servers at CWU connect to approximately two dozen casters around the world to stream raw data into a local key-value store. Ancillary data needed for precise positioning, including smoothed satellite clock and orbit corrections determined by global observations (Dow *et al.*, 2009), earth orientation parameters from the International Earth Rotation and Reference Systems bulletin A (McCarthy, 1996), and the troposphere mapping function of (Boehm *et al.*, 2006) antenna phase center corrections from IGS14 ANTEX and other data products, are ingested using similar methods and retained in a separate key-value store.

CWU's Fastlane software (Santillan *et al.*, 2013) estimates position from GPS-only carrier-phase observables using real-time updates to both the satellite clocks and orbits provided by the real-time service of the International GNSS Service (Dow *et al.*, 2009). Prior to the use for positioning, the carrier-phase data are internally continuously calibrated using a geometry-free combination of the L1 and L2 pseudorange and carrier-phase observables. This calibration step is implemented as a Kalman filter that simultaneously estimates the best floating point ambiguities while monitoring and correcting for breaks in phase tracking, known as cycle slips. To decrease positioning error caused by pseudorange multipath, Fastlane estimates position only using carrier-phase observations, unlike most other PPP algorithms (Kouba and Héroux, 2001; Geng *et al.*, 2019) that rely on both phase and pseudorange when inverting for position. This also halves the number of input observations, reducing matrix size and overall computational load, and translates into smaller latencies. Position and other estimation parameters (receiver clock error, tropospheric water vapor, etc.) are inverted from observations via a physical model represented by a small matrix invertible in microseconds. Because the ancillary data streams do not depend on station number, this framework can be expanded to handle tens of thousands of stations simply by adding additional compute nodes to handle more positioning threads.

Resultant point position streams are held in a high-speed key-value store, inside which vector offsets are computed by subtracting each stations' nominal position (discussed in the following and Fig. 4) from the position estimated at the current epoch and rotated into the local north, east, and vertical reference frames. The solutions are then sent to a message broker (Rostanski *et al.*, 2014) that publishes them to third-party subscribers as geoJSON-serialized messages available in earth center, earth-fixed Cartesian, and north, east, and vertical coordinates that reduce metadata requirements for recipients of the solutions. Subscribed users can request different feeds, each organized into different collections of GNSS stations configured for third-party project needs. USGS ShakeAlert

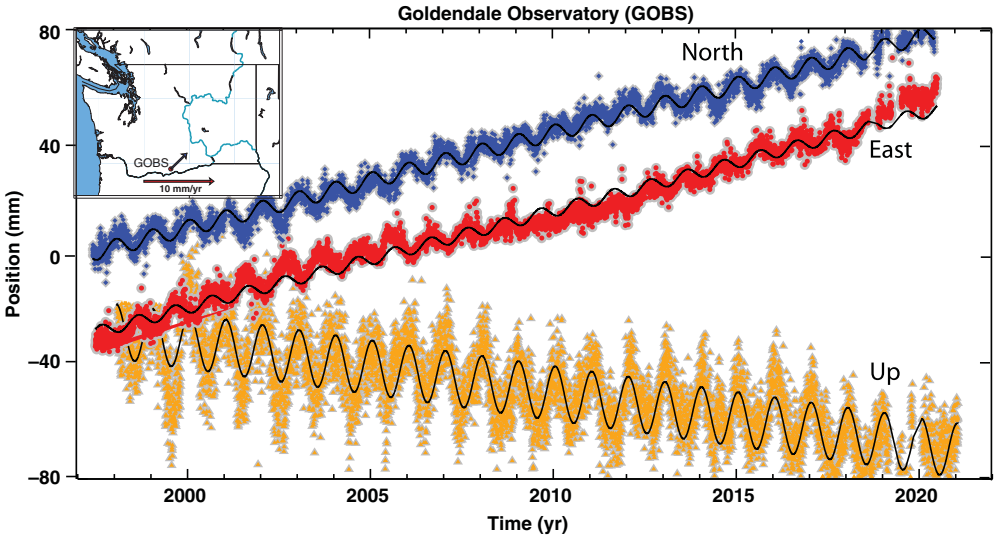

Figure 4. True-of-date nominal positions for PANGA station Goldendale Observatory (GOBS) is computed by extrapolating a trajectory model for each station to the current epoch, updated weekly. Trajectory models comprise linear, sinusoidal, and step function terms to account for steady-state tectonic motion, annual and semiannual oscillatory motions assumed stationary in phase and amplitude, and step functions at times of known earthquakes or hardware changes. Vector velocity map (inset) shows horizontal linear terms of GOBS' trajectory model within the stable North American (NAM14) reference frame.

receives a subset of ~950 stations within, or just outside of, the ShakeAlert footprint polygon of the western United States, National Oceanic and Atmospheric Administration (NOAA) tsunami-warning program receives all global stations near coasts, and USGS National Earthquake Information Center receives all stations positioned. Access to the message broker streams is provided to subscribed users.

PPP solutions also flow to an aggregator that makes waveform position time series available to any browser or other web-based application. Along this path, the data are streamed to a second key-value store, in which it is structured to maintain 5 min, 1 hr, and 24 hr queues of data for all sites that are processed. The 1 and 24 hr queues are decimated to limit the queue size to 600 points. A web application, proxied through a public-facing webserver, accepts URL requests via a defined Application Programmer Interface (API) that returns JSON-serialized position data. Each request is discrete from others, and no request state is maintained on the server, enabling easy balancing of load across multiple instances. Clients make repeated requests for data by including the timestamp of the most recent record they have received, and the response only returns more recently generated solutions. The web API was written specifically to support this functionality. One such client, GPSCockpit (Fig. 5), runs on any web browser and displays vectors that represent the instantaneous position of each station at the current epoch relative to its nominal position. The GPSCockpit client makes requests every 5 s to the CWU aggregator and then redraws the vectors such that, as viewed live, they appear to dance around their nominal position through time. Immediately following a large earthquake, nearby vectors will show their coseismic offset until their trajectory model is updated to include the coseismic step caused by the earthquake.

NOMINAL STATION POSITION

Coseismic offset, or the shift in a GNSS station's position after a nearby earthquake from its nominal position before the earthquake, forms the fundamental basis of GNSS earthquake monitoring. Nominal refers to the station position one would expect at any given epoch in the absence of any transient geophysical process occurring over a ~week or shorter timescale. The global reference frame in which we point position stations is the International Terrestrial Reference Frame (ITRF14; Altamimi *et al.*, 2016) and is updated every few years (Larson, 2019). This frame is centered on Earth's center of mass and rotates with the solid earth. Within ITRF tectonic plates are assumed to translate rigidly at steady state rates well described by Euler poles and rotation rates. Within ITRF, nearly all stations are moving, some at fairly high rates. The western margin of California, for instance, moves roughly 4 cm/yr within ITRF, the inland Pacific Northwest rates average around 3 cm/yr, and some regions around the globe reach nearly 10 cm/yr (Altamimi *et al.*, 2016). Centimeter-level accuracy in seismic monitoring requires the motion of any receiver within ITRF to be updated regularly. We do so by generating a long-term trajectory model for each station, derived from years of past daily measurements of each station's unique trajectory through ITRF, and then extrapolating that trajectory to the current epoch.

Trajectory models comprise the coefficients of functions thought to best characterize the wide array of solid-earth processes known to influence receiver trajectories over periods of months to decades (Bevis *et al.*, 2013). These may be either regional in nature or spatially localized to each site, may arise from natural or anthropogenic origins, and may appear as steady state (linear) or transient (nonlinear) signals through time, all of which must be properly modeled to obtain accurate nominal positions. Regional processes that are effectively linear over decades include glacial isostatic adjustment due to Holocene deglaciation and interseismic tectonic strain accumulation in the absence of local earthquakes, whereas nonlinear processes

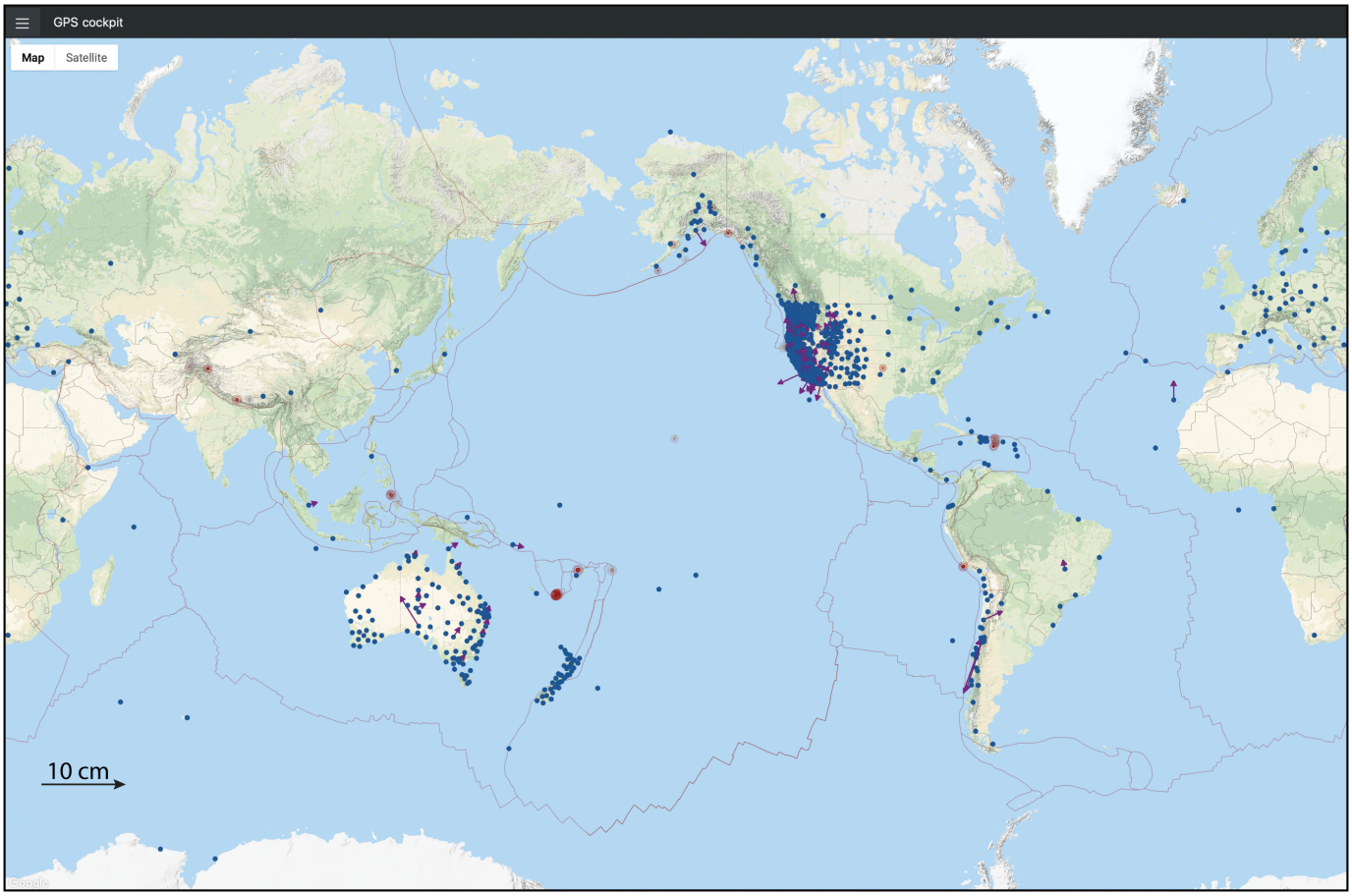

Figure 5. GPSCockpit web application (see Data and Resources) showing instantaneous receiver position offsets from nominal positions, receiver position time series, and fault slip inverted from receiver position time series. The web client, which runs in any browser connected to the Internet, polls the CWU solutions aggregator using a predefined API at a predefined interval (configurable from five second default) to receive the newest position waveforms, computes the vector offsets from nominal position, and renders the vectors at a user-adjustable scale. Vectors appear to dance around their nominal position through time. Other applications permit interactive viewing of GNSS position time series, peak ground deformation contouring, and, where station density permits, continuous inversions for fault slip from third-party estimation routines.

include annual hydrological oscillations either stationary or nonstationary in amplitude or phase, time-dependent anthropogenic aquifer depletion or other resource extraction signals, soil compaction, climatic and ocean loading signals, and numerous others sources, as well as offsets due to tectonic events such as earthquakes, postseismic decay signals following earthquake offsets, as well as numerous others (Dong *et al.*, 2002). Figure 4 shows the trajectory model (black-solid line) for one GNSS station, Goldendale Observatory in Washington State, which comprises the linear term (to account for steady-state tectonic motion), sinusoids of constant phase and amplitude (annual and semiannual signals), step functions (earthquakes or hardware changes to the stations), and logarithmic terms (postseismic decay). Failure to account for the station motion through the reference frame, for instance, by assigning a fixed nominal position, would noticeably degrade centimeter-level accuracy measurement resolution within a matter of weeks for many stations on earth (Bock *et al.*, 2018). Once obtained, the trajectory model may be extrapolated to the current epoch on a regular interval (usually weekly) to provide a current nominal station position. This is then subtracted from instantaneous position to yield a time-dependent station offset.

This highlights one interesting vicissitude of GNSS seismic monitoring. A rule of thumb is that any known signal of which amplitude exceeds 1 mm/yr cannot generally be ignored, which requires that trajectory models be inferred from a minimum of 2–3 yr of continuous observations, given typical noise properties of daily-averaged positions. This means that a newly installed station is not immediately fully useful for seismic monitoring at centimeter accuracy until a trajectory model for it can be derived. Until one is available, short-term workarounds can be used at reduced accuracy, for instance, simply using the previous days' daily position, which requires postprocessing of data, by borrowing a nearby stations' trajectory model, if applicable, or by differencing current position with the average position over a previous interval of a week or two.

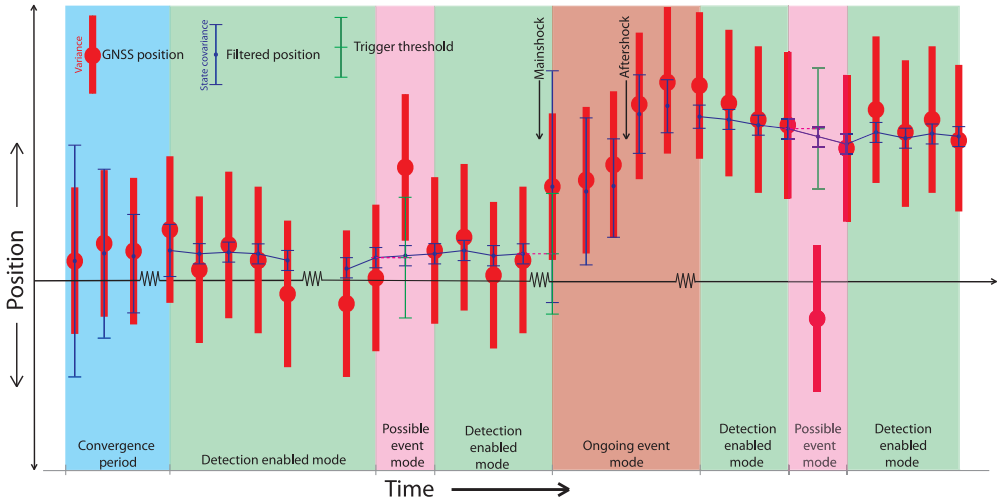

Figure 6. Schematic of coseismic offset filter. Filter is initially incapable of detecting offset during an initial convergence period until its state covariance drops below a threshold level, after which detection is enabled. If solutions exceed a tunable multiple of state covariance, the filter enters into a possible event mode, at which time the previous state is saved. If subsequent solutions regress back to the saved state, the filter re-enters the detection-enabled mode and discards the previous saved state. If subsequent solutions do not regress to the previously saved "possible event" state values, the filter enters into "ongoing event" mode, resets the state covariance, and proceeds to accumulate new solutions until the filter reconverges. Coseismic offset is then the difference between the new state and its previously saved state. Any aftershocks that occur during ongoing event mode and prior to reconvergence of the filter will be included with the mainshock coseismic offset estimate.

COSEISMIC OFFSET ESTIMATION

One approach to evaluating coseismic offsets is to input earthquake hypocenters from seismic networks and zero out all nearby station positions at the origin time of the event, as is done by the PGD algorithm (Crowell *et al.*, 2013). Another approach that can operate independently of seismic hypocenters, which cannot be guaranteed to be available, is to stochastically filter the GNSS position time series and to trigger on offsets that exceed predefined statistical thresholds. This is the approach we take here, such that this GNSS system can operate independently of the existence of a seismic network. For this, we use a two-state memory Kalman filter to estimate coseismic offsets and refer to this later as an "offset filter." Kalman filtering produces the optimal time-dependent least-squares estimate to a model, and extensive discussion of the discipline may be found in Musoff and Zarchan (2009). We model GNSS time series as stochastic processes comprising a constant plus time-variable, non-Gaussian, nonwhite noise, and we assume no correlation between stations or between components of a given station. This is the physically accurate model, because the vast majority of time receivers are not physically moving within the ITRF14 reference frame, apparent position wander is estimation noise, and coseismic deformation may result in any direction depending on an earthquake fault's orientation, rake, and location relative to the station. Other filter approaches are possible, for instance, embedding a known fault geometry and inverting directly for slip along that structure (Segall and Matthews, 1997; McGuire and Segall, 2003).

GNSS point position streams have intrinsic time-dependent colored noise that originates from multiple physical processes acting over a wide range of time and spatial scales (Dong *et al.*, 2002), which require that a time-dependent rate of process noise be added during filter updates to track position drift with time. We tune the addition of process noise such that random-walk drift of the positions is absorbed but transient motions from displacements acting over minutes cannot be absorbed by process noise. The rate of addition uses the post-fit phase residuals from the position estimation subsequently scaled by an additional time-dependent factor derived from the position scatter itself around its nominal position (usually greater than 1) to accommodate unmodeled noise not reflected in formal errors, as discussed in Senko (2018). Dynamic displacements from surface waves and other crustal coda are usually helpful in triggering coseismic offset estimation but complicate estimating coseismic offsets quickly, because reconvergence of the filters is delayed until they disperse. Offset estimation filter instances are created and destroyed automatically downstream of positioning as new GNSS stations are introduced into CWU's global processing system or existing streams time out through any delay long enough to warrant terminating an existing instance.

Figure 6 shows the various states of the filter. Qualitatively, as solutions start flowing for a new station (or recover after a significant outage) the filter state covariance is large, so the filter is not immediately able to detect offsets. As measurements accumulate and the state covariance converges below a predetermined threshold, which typically takes a few tens of seconds, detection of any offset greater than four times the state covariance is enabled. If short-lived anomalous measurements trigger the filter, the filter enters into a "possible event" mode in which the previous state is saved and the state covariance is reset. If new measurements return back to within a predefined range of the saved state, the filter readopts the previously saved state and returns to "detection enabled" mode. If not, the filter enters into an "ongoing event" mode and stays that way until the filter reconverges after sufficient new measurements are accumulated, such that the state covariance once again drops

below the predetermined threshold. Any aftershocks that occur before the filter reconverges out of "ongoing event" mode will be lumped in with the mainshock, because the filter, having not reconverged after the mainshock but prior to the aftershock, cannot differentiate between the two. Once sufficient measurements accumulate so that reconvergence is achieved, coseismic offset is then the difference between the state at the time of reconvergence and the state last saved prior to entering "possible event" mode. In practice, noisier position time series, either through intrinsic positioning noise or because of dynamic displacements, degrade offset detectability of any given size within any given time window, and longer wait times are required for detection at some statistical threshold. This model is built into forward-only Kalman filters with time-dependent statistics designed to ignore drift and trigger on true coseismic motion while minimizing false positives and negatives, and is tuned using a variety of previously GNSS-measured earthquakes, as discussed by Senko (2018).

The system operated as designed during the 2020 M_w 7.1 Ridgecrest, California, earthquake sequence. The M_w 6.4 foreshock did not trigger offset estimation, because the positioning error prior to the event was sufficiently large that the largest coseismic offset, just under 10 cm on the east component of the closest station, was statistically insufficient to trigger the filter. The M_w 7.1 mainshock did trigger offset estimation filters, which subsequently converged within 25 s, as timed by reconvergence interval following stochastic reset (Melbourne *et al.*, 2020). This illustrates a practical lower limit to sparse-network detectability, currently roughly low- to mid-magnitude 6, depending on network geometry, although this magnitude is steadily dropping as improved global models enable lower-scatter positioning, with the ultimate goal of subcentimeter within a global reference frame.

PERFORMANCE

To validate the monitoring system, we developed a parallel data analytics platform to quantify latency, static accuracy, and completeness. To ingest, analyze, and archive the roughly 100 million solutions generated daily per thousand stations positioned, we use an open-source data analytics storage system configured to handle GNSS point position solutions (Betke and Kunkel, 2017). We track a variety of latencies, including telemetry time of data from the receiver to its network caster, transmission time from caster to the CWU positioning system (Fig. 7a), positioning time (Fig. 7b), and arrival time into the position solution transmission exchanges. We cannot track downstream latency to end users such as USGS ShakeAlert decision modules or NOAA but anticipate that to be subsecond.

Figure 7c shows the completeness of solutions as a function of latency. Here, 100% completeness at 1 s epochs assumes 86,400 solutions per day (one position per second) per station positioned. Over the one-week testing interval solutions, completeness within 0.5, 1 and 2 s of acquisition of raw satellite observables in the field is 55%, 90%, and 99%, respectively. Latency, which we define as the time a given epoch's Fastlane position estimation arrives in the solutions key–value store (Fig. 3) minus the time of the epoch itself, is largely independent of station distance from Washington State but appears to be correlated instead with the total number of router hops between the receiver in the field and CWU. For instance, Antarctic stations telemetered over direct satellite links typically show latencies comparable to ethernet-connected receivers in Washington State.

We track static positioning accuracy by computing the deviation of each point position solution from nominal, computed as described previously. Figure 7d–f shows position variance histograms for one typical week for 1250 globally distributed stations, comprising $\sim 7.5 \times 10^8$ total solutions. Horizontal positions are normally distributed with means within 1 cm of 0, showing no consistent biases in the global calculation of nominal positions. Position variances in the north, east, and vertical components are 8, 9, and 12 cm. Most of this scatter is primarily random walk and concentrated in an ~4–5 min period spectral band that originates from errors in satellite clock corrections and most strongly impacts the vertical component (Fig. 7f), but other sources include multipath, second-order ionospheric effects (Kedar *et al.*, 2003), improperly mapped troposphere water delay from zenith, earth orientation, and reference frame errors, among others. The skewness toward the negative seen in the vertical distribution is noteworthy but not easily explainable at this time. This 4–5 min peak noise spectra are discussed in Melgar *et al.* (2020) using 1 yr of measurements for 200 North American stations. They note that for all but the greatest earthquakes that exhibit 4+ min rupture times, and which also typically show many meters of offsets such as the Tohoku 2011 or Indonesia 2004 earthquakes, the overall precision of Fastlane point positions is easily sufficient for characterizing large earthquakes.

DYNAMIC POSITIONING ACCURACY

Accuracy of dynamic positioning, which measures how well GNSS positioning tracks true known motions across different frequencies, is equally important for seismic monitoring but difficult to test without a shake table. In real-time positioning, overdamping time variability will minimize excursions caused by mismodeling any number of error sources and so produce "flatter" time series that, in the absence of true transient ground motion, falsely appear to show higher accuracy and precision (Grapenthin, 2021). Overdamping, however, will render positioning unresponsive to and incapable of accurately tracking rapid dynamic motion, which for earthquakes typically falls in the 2–0.05 Hz range. For the 2019 Ridgecrest mainshock, the dynamic accuracy of the CWU Fastlane real-time positions was vetted three different ways, as discussed in Melbourne *et al.* (2020). First, Fastlane solutions computed in real time during the Ridgecrest mainshock were compared

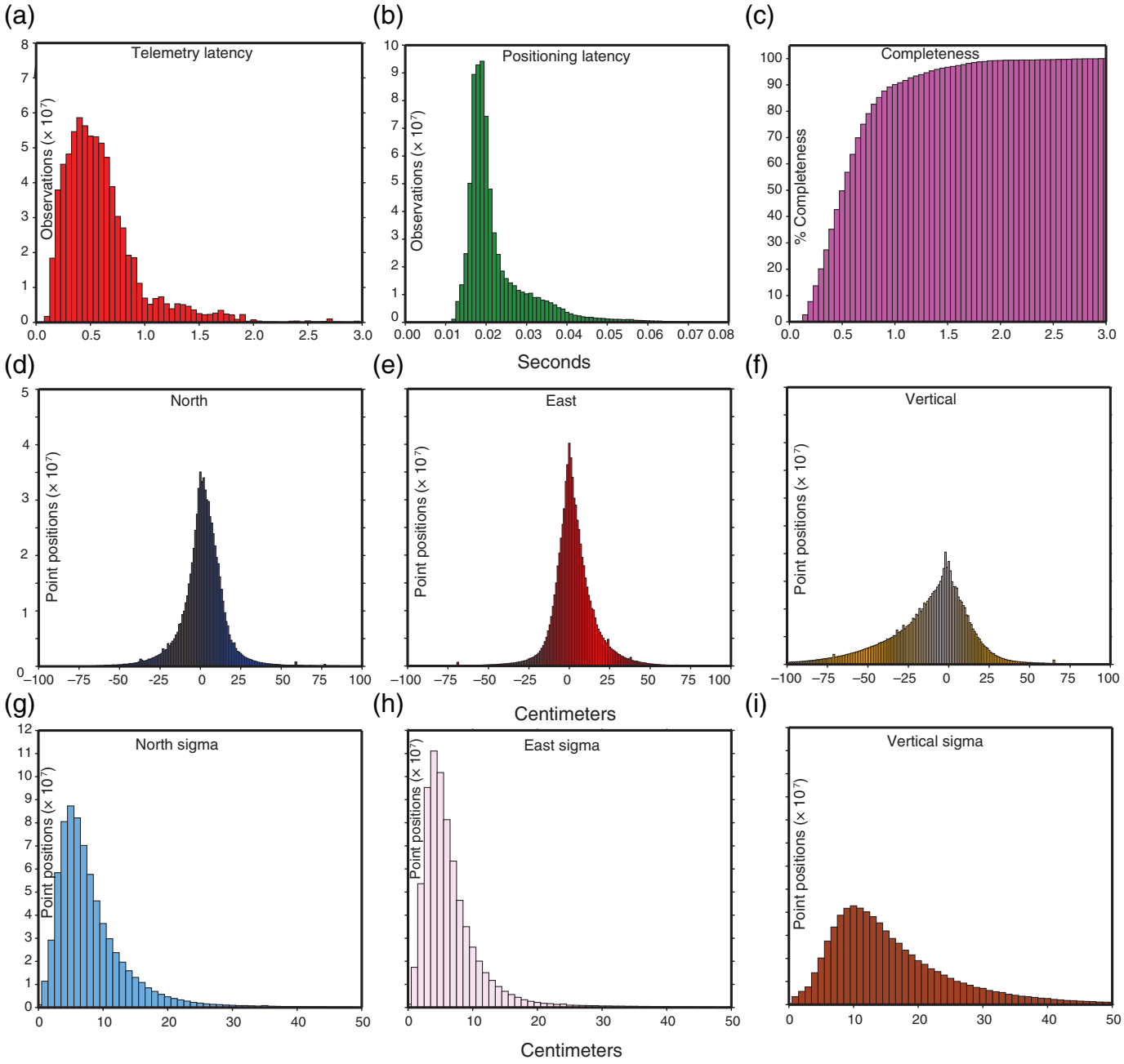

with those computed independently and retroactively using the best possible satellite orbits and clocks, and demonstrated the real-time positioning closely match postprocessed high-rate positioning (Fig. 8a). Second, it was shown that coseismic offsets determined in under 30 s generally agreed with postprocessed coseismic offsets based on 48 hr of data, although were ~10% smaller in magnitude. This discrepancy was noted to be likely due, at least, in part, to true additional deformation contributed by thousands of aftershocks that occurred during the first 48 hr but after the first 30 s after origin time along the same fault strand as the mainshock. Third, the Fastlane position waveforms reasonably matched predictions by the USGS mainshock finite-fault slip distribution within the southern California crustal structure of Hadley and Kanamori (1977).

Figure 7. Fastlane PPP performance analytics measuring latency, completeness, and accuracy for 1270 globally distributed stations positioned during a typical one week period (7–14 July 2020), totaling ~750 million solutions. (a) Telemetry latency is the time of arrival into the observables decoder (Fig. 3) minus observation of time of that epoch. (b) Positioning latency is time of arrival of a solution into the solutions key–value store minus time of arrival of its raw satellite observables into the observables key–value store. (c) Completeness is defined as number of solutions with acceptable covariances through time divided by percentage of maximum number of possible solutions per time (86,400 solutions per 24 hr per receiver for 1 s epochs). (d–f) North, east, and vertical position difference at each epoch from nominal position. (g–i) North, east, and vertical positions formal errors.

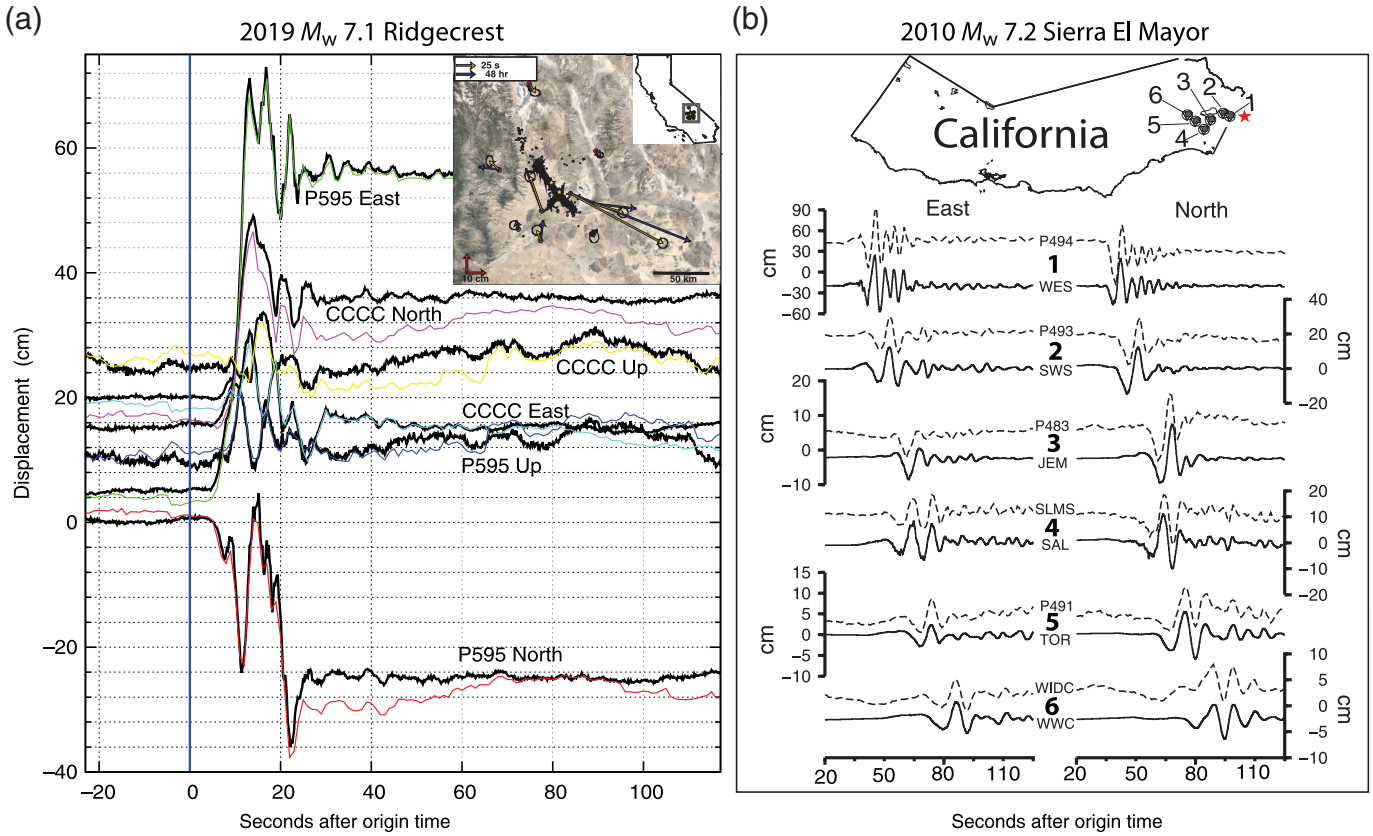

Figure 8. Assessment of Fastlane dynamic positioning accuracy for the (a) 2019 Ridgecrest M_w 7.1 Ridgecrest, California and (b) 2010 M_w 7.2 Sierra El Mayor, Mexico, mainshocks. For Ridgecrest, north, east, and vertical ("Up") positions generated in real time with Fastlane (colored time series) are overlain by postprocessed GipsyX point positions generated using precise satellite orbits and clocks provided by Jet Propulsion Laboratory (Zumberge *et al.*, 1997) (black time series) and analyzed D. Mencin of UNAVCO, Inc. (Mattioli *et al.*, 2020). Inset shows mainshock coseismic offset vectors assessed at 25 s (orange) and 48 hr (blue) after event origin time. For 2010 Sierra El Mayor, GNSS positions (dashed top lines) and double-integrated collocated strong ground motion accelerometer data (solid bottom lines) show a high level of agreement between phase arrival times, amplitudes, and polarity on both north and east components with corresponding GNSS positions. The time axis is seconds after origin time, and the ordinate is in centimeter. Inset. California station map showing location of collocated GPS and accelerometers. Global Positioning System (GPS)–accelerometer station pairs are indicated by the numbered circles: (1) WIDC-WWC, (2) P491-TOR, (3) SLMS-SAL, (4) P483-JEM, (5) P493-SWS, and (6) P494-WES. Mainshock epicenter is shown by the red star.

A fourth method of assessing dynamic accuracy is to compare GNSS position time series with other positioning measurements. For the 2010 M_w 7.2 Sierra El Mayor, Mexico, mainshock, we use double-integrated strong ground motion accelerometer recordings from instruments collocated with, or near, GNSS receivers that also experience strong ground motion. Six station pairs with instrument spacing between 80 m (WES-P494) and 3.6 km (JEM-P483) were used, with the closest pair located approximately 70 km from the epicenter. The GPS–accelerometer pairs are WIDC-WWC, P491-TOR, SLMS-SAL, P483-JEM, P493-SWS, and P494-WES (Fig. 8b). The first motion body-wave amplitudes are small due to the nodal location of the station pairs (310°–330°) relative to the rupture plane of the earthquake (313°). The accelerometer data are corrected for instrument response, double integrated to obtain displacement, and band-pass filtered with a 1-pass Butterworth filter with corner frequencies of 0.1 and 5 Hz. Displacements exceed 40 cm for the east component of the closest accelerometer (WES). The waveform comparisons between GNSS and integrated accelerometer measurements show a high level of agreement between phase arrival times, amplitudes, and polarity that indicate that the GNSS positioning algorithm accurately captures the true ground motion experienced by the GNSS receiver antenna.

DISCUSSION

GNSS position time series from around the globe are now being ingested routinely into USGS National Earthquake Information Center and within NOAA's tsunami warning system as a supplement to global seismic and tide-gauge networks and DART buoy system, whereas the inversions for slip and tsunami excitation estimates are still in the early stages of being vetted and tested (Angove *et al.*, 2019). From a practical standpoint, GNSS receiver installations continue to proliferate and now approach 20,000 stations, only a small fraction of which are publicly available and continuously telemetered (Blewitt

et al., 2018). This expansion is expected to continue as technology evolves, costs decrease, and carrier-phase tracking devices, such as smartphones, continue to accelerate and may, eventually, enable crowd-sourced early warning (Minson *et al.*, 2015). Today, the majority of GNSS existing receivers tend to be concentrated within urbanized regions where the GNSS's unique ability to characterize earthquakes is the most complementary to existing seismic monitoring. This is, particularly, true in tectonic regions where early warning systems are of the greatest societal benefit. However, in addition to the build-out of real-time networks, GNSS seismic monitoring is now possible only due to continual improvements across the discipline, ranging from entirely new satellite constellations to the advent of freely available ancillary corrections to satellite orbits and clocks, without which routine resolution of dynamic ground motions within an Earth center-of-mass reference frame at several centimeter accuracy would not be possible.

Global GNSS seismic monitoring opens up other geophysical risk reduction applications not discussed here. For rupture through dense networks, such as those found in Japan and the western United States, quickly identifying the spatial extent, onset, and amount of static deformation offers a complementary and independent means of estimating of earthquake magnitude as it evolves in real time. This includes tracking rupture as it propagates through the network, in complement to local seismic networks. For subduction events that comprise the majority of seismic moment release globally, real-time inversion of GNSS position waveforms for slip may also be used to compute tsunami excitation. By convolving seafloor uplift predicted from GNSS-derived slip inversions with precomputed hydrodynamic Green's functions, tsunami excitation can be preliminarily assessed without having to wait for teleseismic propagation delays that often exceed local inundation times (Blewitt *et al.*, 2006; Sobolev *et al.*, 2007; Song, 2007; Melgar and Bock, 2013; Angove *et al.*, 2019). Another advantage is that, by being sensitive to all frequencies out to 0 Hz, terrestrial GNSS is sensitive to any slow-rupture component of moment release that is underestimated by conventional global seismic analyses, such as has been documented in tsunami earthquakes (Kanamori and Kikuchi, 1993; Satake, 1995; Ikuta *et al.*, 2015).

Access to existing real-time data streams from existing networks for hazards mitigation purposes remains the biggest issue, going forward. All these applications depend on getting data; as Figure 2 shows, the number of operating GNSS stations vastly outstrips the number of stations available publicly today. Efforts are underway to promote open-data policies, such as those on which global tide gauge data are exchanged (LaBrecque *et al.*, 2019).

DATA AND RESOURCES

Global Navigational Satellite System (GNSS) data shown in Figure 8 were collected as part of the Network of the Americas operated by UNAVCO, Inc. Receiver Independent Exchange Format (RINEX) data may be retrieved from www.unavco.org/data/gps-gnss/data-access-methods/data-access-methods.html. GNSS time series in Figure 1, other than the 2011 Tohoku earthquake, are from Ruhl *et al.* (2018). Figures were generated with Gnuplot and Generic Mapping Tools (Wessel and Smith, 1991). The GPSCockpit web application is available at www.panga.org/realtime/gpscockpit. All websites were last accessed in April 2021.

DECLARATION OF COMPETING INTERESTS

The authors acknowledge that there are no conflicts of interest recorded.

ACKNOWLEDGMENTS

All coauthors of this article contributed equal and complementary efforts. Development of global Global Navigational Satellite System (GNSS) seismic analyses is supported by National Aeronautics and Space Administration (NASA)–Environmental Seismic Intensity (ESI) Awards NNX14AQ40G and 80NSSC19K0359 and U.S. Geological Survey Cooperative Agreements G17AC00344 and G19AC00264 to Central Washington University. Data from the Network of the Americas are provided by the Geodetic Facility for the Advancement of Geoscience (GAGE) Facility, operated by UNAVCO, Inc., with support from the National Science Foundation (NSF) and NASA under NSF Cooperative Agreement EAR-1724794. Constructive reviews were provided by Dr. Kathleen Hodgkinson of UNAVCO, Inc. and Drs. Ronni Grapenthin and Michael West of University of Alaska, Fairbanks.

REFERENCES

Aagaard, B. T., G. Anderson, and K. W. Hudnut (2004). Dynamic rupture modeling of the transition from thrust to strike-slip motion in the 2002 Denali fault earthquake, Alaska, *Bull. Seismol. Soc. Am.* **94,** no. 6B, S190–S201.

Aki, K., and P. G. Richards (1980). *Quantitative Seismology: Theory and Methods*, 932 pp.

Allen, R. M., and A. Ziv (2011). Application of real-time GPS to earthquake early warning, *Geophys. Res. Lett.* **38,** no. 16, doi: 10.1029/2011GL047947.

Altamimi, Z., P. Rebischung, L. Métivier, and X. Collilieux (2016). ITRF2014: A new release of the International Terrestrial Reference Frame modeling nonlinear station motions, *J. Geophys. Res.* **121,** no. 8, 6109–6131.

Angove, M., D. Arcas, R. Bailey, P. Carrasco, D. Coetzee, B. Fry, K. Gledhill, S. Harada, C. von Hillebrandt-Andrade, L. Kong, *et al.* (2019). Ocean observations required to minimize uncertainty in global tsunami forecasts, warnings, and emergency response, *Front. Mar. Sci.* **6,** no. 350, doi: 10.3389/fmars.2019.00350.

Barnhart, W. D., G. P. Hayes, and R. D. Gold (2019). The July 2019 Ridgecrest, California, earthquake sequence: Kinematics of slip and stressing in cross-fault ruptures, *Geophys. Res. Lett.* **46,** no. 21, 11,859–11,867.

Berglund, H. T., F. Blume, and A. Prantner (2015). Effects of earthquake ground motion on tracking characteristics of new Global Navigation Satellite System receivers, *Geophys. Res. Lett.* **42,** no. 9, 3282–3288.

Betke, E., and J. Kunkel (2017). *Real-Time I/O-Monitoring of HPC Applications with SIOX, Elasticsearch, Grafana and FUSE*, Springer International Publishing, Cham, Switzerland, 174–186.

Bevis, M., A. Brown, and E. Kendrick (2013). Devising stable geometrical reference frames for use in geodetic studies of vertical crustal motion, *J. Geodes.* **87,** no. 4, 311–321.

Blewitt, G., W. C. Hammond, and C. Kreemer (2018). Harnessing the GPS data explosion for interdisciplinary science, *Eos Trans. AGU* **99,** doi: 10.1029/2018EO104623.

Blewitt, G., W. C. Hammond, C. Kreemer, H.-P. Plag, R. S. Stein, and E. Okal (2009). GPS for real-time earthquake source determination and tsunami warning systems, *J. Geodes.* **83,** 335–343.

Blewitt, G., C. Kreemer, W. C. Hammond, H.-P. Plag, S. Stein, and E. Okal (2006). Rapid determination of earthquake magnitude using GPS for tsunami warning systems, *Geophys. Res. Lett.* **33,** no. 11, doi: 10.1029/2006GL026145.

Blewitt, G., R. P. Malla, M. B. Heflin, F. H. Webb, and U. J. Lindqwister (1992). Global coordinates with centimeter accuracy in the International Terrestrial Reference Frame using GPS, *Geophys. Res. Lett.* **19,** no. 9, 853–856.

Bock, Y., P. Fang, and G. F. Helmer (2018). California spatial reference system: CSRS epoch 2017.50 (NAD83), *Final Rept.*, California Department of Transportation (Caltrans), Sacramento, California, Report Number 1.

Boehm, J., A. Niell, P. Tregoning, and H. Schuh (2006). Global Mapping Function (GMF): A new empirical mapping function based on numerical weather model data, *Geophys. Res. Lett.* **33,** no. 7, doi: 10.1029/2005GL025546.

Caskey, S. J., S. G. Wesnousky, P. Zhang, and D. B. Slemmons (1996). Surface faulting of the 1954 Fairview Peak (M_s 7.2) and Dixie Valley (M_s 6.8) earthquakes, central Nevada, *Bull. Seismol. Soc. Am.* **86,** no. 3, 761–787.

Crowell, B. W., Y. Bock, and D. Melgar (2012). Real-time inversion of GPS data for finite fault modeling and rapid hazard assessment, *Geophys. Res. Lett.* **39,** no. 9, doi: 10.1029/2012GL051318.

Crowell, B. W., D. Melgar, Y. Bock, J. S. Haase, and J. Geng (2013). Earthquake magnitude scaling using seismogeodetic data, *Geophys. Res. Lett.* **40,** no. 23, 6089–6094.

Dong, D., P. Fang, Y. Bock, M. K. Cheng, and S. Miyazaki (2002). Anatomy of apparent seasonal variations from GPS-derived site position time series, *J. Geophys. Res.* **107,** no. B4, ETG-9.

Dow, J. M., R. E. Neilan, and C. Rizos (2009). The International GNSS Service in a changing landscape of Global Navigation Satellite Systems, *J. Geodes.* **83,** no. 3, 191–198.

Ebinuma, T., and T. Kato (2012). Dynamic characteristics of very-high-rate GPS observations for seismology, *Earth Planets Space* **64,** no. 5, 369–377.

Espinosa-Aranda, J. M., A. Cuéllar, F. H. Rodríguez, B. Frontana, G. Ibarrola, R. Islas, and A. García (2011). The seismic alert system of Mexico (SASMEX): Progress and its current applications, *Soil Dynam. Earthq. Eng.* **31,** no. 2, 154–162.

Geng, J., X. Chen, Y. Pan, S. Mao, C. Li, J. Zhou, and K. Zhang (2019). PRIDE PPP-AR: An open-source software for GPS PPP ambiguity resolution, *GPS Solutions* **23,** no. 4, 1–10.

Given, D. D., R. M. Allen, A. S. Baltay, P. Bodin, E. S. Cochran, K. Creager, R. M. de Groot, L. S. Gee, E. Hauksson, T. H. Heaton, *et al.* (2018). Revised technical implementation plan for the ShakeAlert system—An earthquake early warning system for the west coast of the United States, *U.S. Geol. Surv. Open-File Rept. 2018-1155*, 42 pp.

Grapenthin, R. (2021). The Global Navigation Satellite System (GNSS): Positioning, velocities, and reflections, in *Remote Sensing Applications to Geohazards and Natural Resources*, E. Chaussard (Editor), Springer, New York, New York.

Grapenthin, R., I. Johanson, and R. M. Allen (2014a). The 2014 Mw 6.0 Napa earthquake, California: Observations from real-time GPS-enhanced earthquake early warning, *Geophys. Res. Lett.* **41,** no. 23, 8269–8276.

Grapenthin, R., I. A. Johanson, and R. M. Allen (2014b). Operational real-time GPS-enhanced earthquake early warning, *J. Geophys. Res.* **119,** no. 10, 7944–7965.

Hadley, D., and H. Kanamori (1977). Seismic structure of the transverse ranges, California, *GSA Bull.* **88,** no. 10, 1469–1478.

Hayes, G. P., P. S. Earle, H. M. Benz, D. J. Wald, R. W. Briggs, and , and The USGS/NEIC Earthquake Response Team (2011). 88 hours: The U.S. Geological Survey National Earthquake Information Center response to the 11 March 2011 M_w 9.0 Tohoku earthquake, *Seismol. Res. Lett.* **82,** no. 4, 481–493.

Herring, T. (2002). *TRACK GPS Kinematic Positioning Program*, version 1.07, Massachusetts Institute of Technology, Cambridge, Massachusetts.

Hodgkinson, K. M., D. J. Mencin, K. Feaux, C. Sievers, and G. S. Mattioli (2020). Evaluation of earthquake magnitude estimation and event detection thresholds for real-time GNSS networks: Examples from recent events captured by the network of the Americas, *Seismol. Res. Lett.* **91,** no. 3, 1628–1645.

Hoshiba, M., K. Iwakiri, N. Hayashimoto, T. Shimoyama, K. Hirano, Y. Yamada, Y. Ishigaki, and H. Kikuta (2011). Outline of the 2011 off the Pacific coast of Tohoku Earthquake (M_w 9.0)—Earthquake early warning and observed seismic intensity, *Earth Planets Space* **63,** no. 7, 547–551.

Hudnut, K. W., G. J. Anderson, A. Aspiotes, N. E. King, R. A. Moffitt, and K. F. Stark (2002). GPS fault slip sensors, *Asia–Pacific Economic Cooperation Symposium*, Taipei, Taiwan, 28–29 November.

Ikuta, R., Y. Mitsui, Y. Kurokawa, and M. Ando (2015). Evaluation of strain accumulation in global subduction zones from seismicity data, *Earth Planets Space* **67,** no. 1, 1–17.

Kanamori, H., and M. Kikuchi (1993). The 1992 Nicaragua earthquake: A slow tsunami earthquake associated with subducted sediments, *Nature* **361,** 714–716.

Kawamoto, S., Y. Hiyama, Y. Ohta, and T. Nishimura (2016). First result from the GEONET real-time analysis system (REGARD): The case of the 2016 Kumamoto earthquakes, *Earth Planets Space* **68,** no. 1, 1–12.

Kedar, S., G. A. Hajj, B. D. Wilson, and M. B. Heflin (2003). The effect of the second order GPS ionospheric correction on receiver positions, *Geophys. Res. Lett.* **30,** no. 16, 2-1–2-4.

Kong, L. S. L., P. K. Dunbar, N. S. Arcos, and International Tsunami Information Center (2015). *Pacific Tsunami Warning System: A Half-century of Protecting the Pacific 1965-2015*, U.S. Government Publishing Office, International Tsunami Information Center, Honolulu, Hawaii.

Kouba, J., and P. Héroux (2001). Precise point positioning using IGS orbit and clock products, *GPS Solutions* **5,** no. 2, 12–28.

LaBrecque, J., J. B. Rundle, and G. W. Bawden (2019). Global navigation satellite system enhancement for tsunami early warning systems,

Global Assessment Report on Disaster Risk Reduction, UN Office for Disaster Risk Reduction, available at https://www.undrr.org/publication/global-navigation-satellite-system-enhancement-tsunami-early-warning-systems (last accessed April 2021).

Larson, K. M. (2019). Unanticipated uses of the Global Positioning System, *Annu. Rev. Earth Planet. Sci.* **47,** no. 1, 19–40.

Larson, K. M., P. Bodin, and J. Gomberg (2003). Using 1-Hz GPS data to measure deformations caused by the Denali fault earthquake, *Science* **300,** no. 5624, 1421–1424.

Leick, A., L. Rapoport, and D. Tatarnikov (2015). *GPS Satellite Surveying*, John Wiley & Sons, Inc, Hoboken, New Jersey, 1–840.

Mattioli, G. S., D. A. Phillips, K. M. Hodgkinson, C. Walls, D. J. Mencin, B. A. Bartel, D. J. Charlevoix, C. Crosby, M. J. Gottlieb, B. Henderson, *et al.* (2020). The GAGE data and field response to the 2019 Ridgecrest earthquake sequence, *Seismol. Res. Lett.* **91,** no. 4, 2075–2086, doi: 10.1785/0220190283.

McCarthy, D. D. (1996). IERS conventions (1996), *IERS Technical Note 21*, 1–95.

McGuire, J. J., and P. Segall (2003). Imaging of aseismic fault slip transients recorded by dense geodetic networks, *Geophys. J. Int.* **155,** no. 3, 778–788.

Melbourne, T. I., W. M. Szeliga, V. M. Santillan, and C. W. Scrivner (2020). 25-second determination of 2019 M_w 7.1 Ridgecrest earthquake coseismic deformation, *Bull. Seismol. Soc. Am.* **110,** no. 4, 1680–1687.

Melgar, D., and Y. Bock (2013). Near-field tsunami models with rapid earthquake source inversions from land- and ocean-based observations: The potential for forecast and warning, *J. Geophys. Res.* **118,** no. 11, 5939–5955.

Melgar, D., and G. P. Hayes (2019). Characterizing large earthquakes before rupture is complete, *Sci. Adv.* **5,** no. 5, eaav2032.

Melgar, D., B. W. Crowell, J. Geng, R. M. Allen, Y. Bock, S. Riquelme, E. M. Hill, M. Protti, and A. Ganas (2015). Earthquake magnitude calculation without saturation from the scaling of peak ground displacement, *Geophys. Res. Lett.* **42,** no. 13, 5197–5205.

Melgar, D., B. W. Crowell, T. I. Melbourne, W. M. Szeliga, M. Santillan, and C. W. Scrivner (2020). Noise characteristics of operational real-time high-rate GNSS positions in a large aperture network, *J. Geophys. Res.* **125,** doi: 10.1029/2019JB019197.

Minson, S. E., B. A. Brooks, C. L. Glennie, J. R. Murray, J. O. Langbein, S. E. Owen, T. H. Heaton, R. A. Iannucci, and D. L. Hauser (2015). Crowdsourced earthquake early warning, *Sci. Adv.* **1,** no. 3, e1500036.

Minson, S. E., J. R. Murray, J. O. Langbein, and J. S. Gomberg (2014). Real-time inversions for finite fault slip models and rupture geometry based on high-rate GPS data, *J. Geophys. Res.* **119,** no. 4, 3201–3231.

Murray, J. R., B. W. Crowell, R. Grapenthin, K. Hodgkinson, J. O. Langbein, T. Melbourne, D. Melgar, S. E. Minson, and D. A. Schmidt (2018). Development of a geodetic component for the U.S. west coast earthquake early warning system, *Seismol. Res. Lett.* **89,** no. 6, 2322–2336.

Musoff, H., and P. Zarchan (2009). *Fundamentals of Kalman Filtering: A Practical Approach*, Third Ed., American Institute of Aeronautics and Astronautics, Reston, Virginia, 1–877.

Ohta, Y., T. Kobayashi, H. Tsushima, S. Miura, R. Hino, T. Takasu, H. Fujimoto, T. Iinuma, K. Tachibana, T. Demachi, *et al.* (2012). Quasi real-time fault model estimation for near-field tsunami forecasting based on RTK-GPS analysis: Application to the 2011 Tohoku-Oki earthquake (M_w 9.0), *J. Geophys. Res.* **117,** no. B2, doi: 10.1029/2011JB008750.

Ross, Z. E., B. Idini, Z. Jia, O. L. Stephenson, M. Zhong, X. Wang, Z. Zhan, M. Simons, E. J. Fielding, S.-H. Yun, *et al.* (2019). Hierarchical interlocked orthogonal faulting in the 2019 Ridgecrest earthquake sequence, *Science* **366,** no. 6463, 346–351.

Rostanski, M., K. Grochla, and A. Seman (2014). Evaluation of highly available and fault-tolerant middleware clustered architectures using RabbitMQ, *Proc. 2014 Federated Conf. on Computer Science and Information Systems*, 7–10 September 2014, 879–884.

Ruhl, C. J., D. Melgar, J. Geng, D. E. Goldberg, B. W. Crowell, R. M. Allen, Y. Bock, S. Barrientos, S. Riquelme, J. C. Baez, *et al.* (2018). A global database of strong-motion displacement GNSS recordings and an example application to PGD scaling, *Seismol. Res. Lett.* **90,** no. 1, 271–279.

Santillan, V. M., T. I. Melbourne, W. M. Szeliga, and C. W. Scrivner (2013). A fast-convergence stream editor for real-time precise point positioning, *Annual Meeting of the American Geophysical Union*, San Francisco, California, 9–13 December 2013, G53B–0930.

Satake, K. (1995). Mechanism of the 1992 Nicaragua tsunami earthquake, *Geophys. Res. Lett.* **21,** 2519–2522.

Segall, P., and M. Matthews (1997). Time dependent inversion of geodetic data, *J. Geophys. Res.* **102,** no. 10, 22,391–22,409.

Senko, J. (2018). Slip estimation from real-time GPS in Cascadia, *Master's Thesis*, Central Washington University, 132 pp.

Sobolev, S. V., A. Y. Babeyko, R. Wang, A. Hoechner, R. Galas, M. Rothacher, D. V. Sein, J. Schröter, J. Lauterjung, and C. Subarya (2007). Tsunami early warning using GPS–shield arrays, *J. Geophys. Res.* **112,** no. B8, doi: 10.1029/2006JB004640.

Song, Y. T. (2007). Detecting tsunami genesis and scales directly from coastal GPS stations, *Geophys. Res. Lett.* **34,** no. 19, doi: 10.1029/2007GL031681.

Wessel, P., and W. H. F. Smith (1991). Free software helps map and display data, *Eos Trans. AGU* **72,** no. 41, 441–446.

Wright, T. J., N. Houlié, M. Hildyard, and T. Iwabuchi (2012). Real-time, reliable magnitudes for large earthquakes from 1 Hz GPS precise point positioning: The 2011 Tohoku-Oki (Japan) earthquake, *Geophys. Res. Lett.* **39,** no. 12, doi: 10.1029/2012GL051894.

Zumberge, J. F., M. B. Heflin, D. C. Jefferson, M. M. Watkins, and F. H. Webb (1997). Precise point positioning for the efficient and robust analysis of GPS data from large networks, *J. Geophys. Res.* **102,** no. 3, 5005–5017.

Manuscript received 4 November 2020
Published online 11 May 2021